Front. Earth Sci. 2022, 16(1): 175–189
https://doi.org/10.1007/s11707-020-0849-6

RESEARCH ARTICLE

Estimation of marine winds in and around typhoons using multi-platform satellite observations: Application to Typhoon Soulik (2018)

Seung-Woo LEE[1], **Sung Hyun NAM** (✉)[1,2], **Duk-Jin KIM**[1]

1 School of Earth and Environmental Sciences, College of Natural Sciences, Seoul National University, Seoul 08826, Republic of Korea
2 Research Institution of Oceanography, College of Natural Sciences, Seoul National University, Seoul 08826, Republic of Korea

Abstract Estimating horizontal winds in and around typhoons is important for improved monitoring and prediction of typhoons and mitigating their damages. Here, we present a new algorithm for estimating typhoon winds using multiple satellite observations and its application to Typhoon Soulik (2018). Four kinds of satellite remote sensing data, along with their relationship to typhoon intensity, derived statistically from hundreds of historical typhoon cases, were merged into the final product of typhoon wind (MT wind): 1) geostationary-satellite-based infrared images (IR wind), 2) passive microwave sounder (MW wind), 3) feature-tracked atmospheric motion vectors, and 4) scatterometer-based sea surface winds (SSWs). The algorithm was applied to two cases (A and B) of Typhoon Soulik and validated against SSWs independently retrieved from active microwave synthetic aperture radar (SAR) and microwave radiometer (AMSR2) images, and vertical profiles of wind speed derived from reanalyzed data and dropsonde observations. For Case A (open ocean), the algorithm estimated the realistic maximum wind, radius of maximum wind, and radius of 15 m/s, which could not be estimated using the reanalysis data, demonstrating reasonable and practical estimates. However, for Case B (when the typhoon rapidly weakened just before making landfall in the Korean Peninsula), the algorithm significantly overestimated the parameters, primarily due to the overestimation of typhoon intensity. Our study highlights that realistic typhoon winds can be monitored continuously in real-time using multiple satellite observations, particularly when typhoon intensity is reasonably well predicted, providing timely analysis results and products of operational importance.

Keywords sea surface wind, multi-platform satellites, Typhoon Soulik (2018)

1 Introduction

Typhoons are among the most devastating natural disasters, as they are accompanied by strong winds that often cause severe damage. Therefore, monitoring and predicting the horizontal wind field in and around typhoons is important. However, monitoring and accurate prediction of typhoon intensity are difficult because typhoons occasionally intensify or decay rapidly upon interacting with the underlying ocean. For example, Typhoon Soulik (2018) formed over the tropical western Pacific on August 15–16, moved into the East China Sea from August 21–22, and landed on the Korean Peninsula in August 23, 2018, maintaining its high intensity (Category 5) until rapidly decaying over the northern East China Sea just before landing (Fig. 1(a)). The rapid decay was not well recognized early, and the intensity at that time was overestimated. The decay could be related to two-way interactions between the typhoon and strongly (~6.2°C) cooled, large cold wakes at the sea surface for a sufficiently long period of time due to its slow translation (Park et al., 2019). A strong energy loss from the typhoon into the East China Sea caused its rapid decay just before landing, raising confusion in the public as well as scientific community.

Due to the lack of in situ measurements, observation and monitoring of marine winds across the global oceans, including areas in and around typhoons, dominantly rely on satellite remote sensing products, such as sea surface winds (SSWs) and atmospheric motion vectors (AMVs) (Nam and Park, 2018). Although technologically advanced multiple-satellite missions and wind retrieving techniques have increased the quantity and quality of such products,

Received May 19, 2020; accepted October 27, 2020

E-mail: namsh@snu.ac.kr

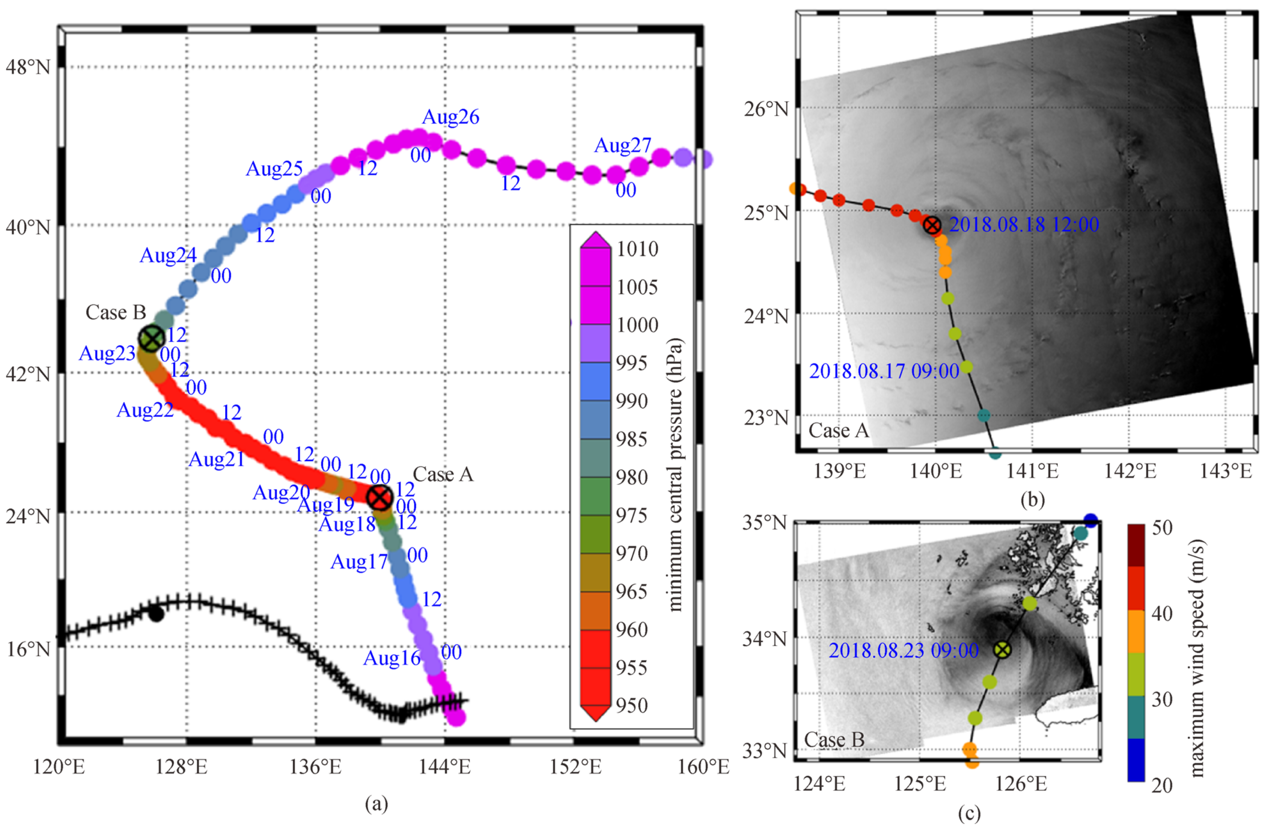

Fig. 1 (a) Typhoon Soulik track with minimum central pressure (colored circles). SAR images taken at (b) 08:38 UTC on 18 August (Case A) and (c) 09:39 UTC on 23 August 2018 (Case B). The location of dropsonde observations at 22:27 UTC on 17 October 2010 is denoted with a black circle in (a) along with the trajectory of the corresponding Typhoon Megi. In (b) and (c), positions of typhoon centers are colored with maximum wind speeds.

there are fundamental limitations posed by the sampling of polar-orbit satellite sensors, such as scatterometers and microwave radiometers. In particular, the horizontal wind field associated with typhoons or typhoon wind has rarely been monitored continuously in real-time. SSWs retrieved from scatterometers have inevitable spatio-temporal gaps, in addition to the systematic over- or underestimation of wind speed (direction) in a regime of high (low) wind speed and rain contamination (Portabella et al., 2012a; Chou et al., 2013). The SSW speeds retrieved from microwave radiometers have an advantage in higher wind retrievals because an increase in sea surface emissivity is physically related to the observed brightness temperature (Wentz, 1997; Mears et al., 2001). Yet, data from microwave radiometers are also limited by spatio-temporal sampling gaps from the polar-orbit. The AMVs derived from geostationary satellites, on the other hand, are rather temporally continuous but spatially very sparse, mostly limited to the upper levels, and removed in the vicinity of typhoons via general quality control (Velden et al., 1997). Several attempts have been made to develop an operationally applicable algorithm for estimating typhoon (hurricane) winds utilizing routinely available IR images from geostationary satellites (Mueller et al., 2006; Knaff et al., 2015), incorporating temperature and geopotential height fields from advanced microwave sounding units (AMSU) using the nonlinear balance equation (Demuth et al., 2004 and 2006; Bessho et al., 2006), and objectively merging data collected from multiple satellite platforms and sensors, including scatterometer-based SSWs and feature-tracked AMVs (Knaff et al., 2011). However, the development of an operationally applicable algorithm for estimating the realistic three-dimensional field of typhoon winds continuously in real-time using multiple satellite observations is still far from complete (Nam and Park, 2018).

This paper presents a new algorithm for estimating the three-dimensional field of horizontal winds in and around typhoons using four kinds of satellite remote sensing products and its application to Typhoon Soulik. The data used and the proposed algorithm are described in Sections 2 and 3, respectively. The application of the algorithm to two cases of Soulik and a discussion are given in Sections 4 and 5, and the conclusions are drawn in Section 6.

2 Data

To estimate the wind field (including SSW) associated with Typhoon Soulik, we used cloud top temperature (CTT) and

AMVs continuously derived from the Communication, Ocean, and Meteorological Satellite (COMS), brightness temperature collected from NOAA-15 AMSU-A, and SSWs at the height of 10 m above sea level retrieved from MetOp-A and-B ASCAT for the area within 600 km from the typhoon center at or closest to 11:11:51 UTC 18 August 2018 and 00:54:01 UTC 23 August 2018, for which the ASCAT data are available. The COMS CTT data have a horizontal resolution of 4 km and sampling time interval of 15 min (Choi et al., 2007 and 2014). The horizontal AMVs at the allocated heights are derived from feature-tracking of successive infrared, shortwave infrared, and water vapor channel images of COMS (Kim and Ou, 2013). The AMVs with a quality index exceeding 0.50 yield a root mean squared error of ~7.6 m/s, regardless of distance from the typhoon center, based on the validation with radiosonde observations (Sohn et al., 2012; Kim and Ou, 2013). Root mean squared errors in the height assignment of the AMVs using the Cloud-Aerosol Lidar and Infrared Pathfinder Satellite Observation cloud mask are ~300 hPa (Sohn et al., 2012). AMSU-A typically collects brightness temperature data 1 to 4 times per day; the data correspond to a swath within 700 km and a horizontal resolution of ~50 km at nadir in two channels: Channel 7 (54940.64 MHz) and Channel 8 (55498.70 MHz). ASCAT operates in the C-band (5.225 GHz) and is less sensitive to rain contamination than Ku-band scatterometers, such as QuikSCAT, but have a higher spatial resolution (~25 km) (Figa-Saldaña et al., 2002; EUMETSAT, 2019).

To determine the statistical relationship of typhoon wind parameters and typhoon intensity, global reanalysis data from the European Centre for Medium-Range Weather Forecasts (ECMWF) for a particular period — Year of Tropical Convection (YOTC) — were used. The ECMWF YOTC data have a relatively high horizontal resolution of 0.125° and a time interval of 6 h from May 2008 to April 2010 (Moncrieff et al., 2012; Waliser et al. 2012). Zonal and meridional winds at 25 pressure levels and at the height of 10 m above sea level within a domain of 10° × 10° centered around 26 typhoons, with a total of 646 time steps, except cases at genesis or extinction steps, were utilized here. Among the 646 historical typhoons, there are 133 cases, for which microwave sounder data in the typhoon-centric domain of 10° × 10° area within a time window of 12 h are simultaneously available. The position of the typhoon center at a resolution of 0.1° and maximum wind speed ($V_{\max}$, m/s) at an interval of 6 h were determined based on the best track data from the Regional Specialized Meteorological Center of the Japan Meteorological Agency in Tokyo (Kunitsugu, 2012).

To validate the SSWs at the height of 10 m above sea level estimated from the developed algorithm for Typhoon Soulik, we used two SAR images taken by Sentinel-1B at 08:38 UTC on 18 August 2018 (Case A; Fig. 1(b)) and Sentinel-1A SAR at 09:39 UTC on 23 August 2018 (Case B; Fig. 1(c)). Specification of SAR images are provided in Table 1. To calculate the backscattering coefficient from the Sentinel-1A and B Ground Range Detected (GRD) product, the following equation was used (CLS, 2019):

$$\sigma^0 = \frac{|DN_i|^2}{A_i^2},$$

where DN is the digital number recorded in the GRD product, and A is the look-up table for sigma-nought stored in the annotation file. After calculating the backscattering coefficients for the two SAR images, SSWs were estimated by applying the CMOD_IFR2 model (IFREMER-CERSAT, 1996). The wind directions and incidence angles required for CMOD_IFR2 were obtained from the ECMWF reanalysis data and annotation file, respectively. The 5th generation of ECMWF reanalysis (ERA5) data at the height of 10 m above sea level and standard pressure levels were used to compare the SSWs and vertical profiles in and around Typhoon Soulik. The ERA5 data have a horizontal resolution of ~30 km and a time interval of 1 h (Olauson, 2018). The wind speed at the height of 10 m above sea level of the Japanese Advanced Microwave Scanning Radiometer 2 (AMSR2) sensor on board the Global Change Observation Mission-Water 1 (GCOM-W1) satellite was retrieved using the GCOM-W1 AMSR-2 Algorithm Software Processor (GAASP). Details are described in the Community Satellite Processing Package site (available at Community Satellite Processing Package website). To validate the vertical profile of the wind speed estimated from the developed algorithm and ERA5, we used the dropsonde data, available from National Oceanic and Atmospheric Administration/Hurricane Research Division online GPS-dropsonde data archive (available at NOAA website), collected at 22:27 UTC on 17 October 2010 in the vicinity of the center of Typhoon Megi.

3 Methods

3.1 Typhoon wind from geostationary satellite infrared images (IR wind)

The algorithm for estimating the three-dimensional field of horizontal wind from IR images of COMS, defined as IR wind, is shown in Fig. 2. The inputs of IR wind were the center position and typhoon intensity, and CTT from the geostationary satellite (Mueller et al., 2006). The IR wind applies a modified Rankine vortex model to represent tangential wind as a function of distance from the typhoon center as below (Fig. 3(a)).

$$V(r) = V_{\max}\left(\frac{r}{R_{\max}}\right), \quad (\text{for } r < R_{\max})$$

$$V(r) = V_{\max}\left(\frac{R_{\max}}{r}\right)^x, \quad (\text{for } r > R_{\max}) \tag{1}$$

Table 1 Specification of SAR images

Satellite name	**Case A**: Sentinel-1B	**Case B**: Sentinel-1A
Acquisition time	2018/08/18 08:38 UTC	2018/08/23 09:39 UTC
Band	C-band (5.405 GHz)	C-band (5.405 GHz)
Orbit direction	Ascending	Ascending
Imaging mode	Extra Wide Swath (EW)	Interferometric Wide Swath (IW)
Polarization	VV + VH	VV + VH
Incidence angle	29.0–47.0°	30.7–46.0°
Swath	400 km	250 km
Resolution (Range × Azimuth)	25 m × 100 m	5 m × 20 m
Noise floor	−22 dB	−22 dB

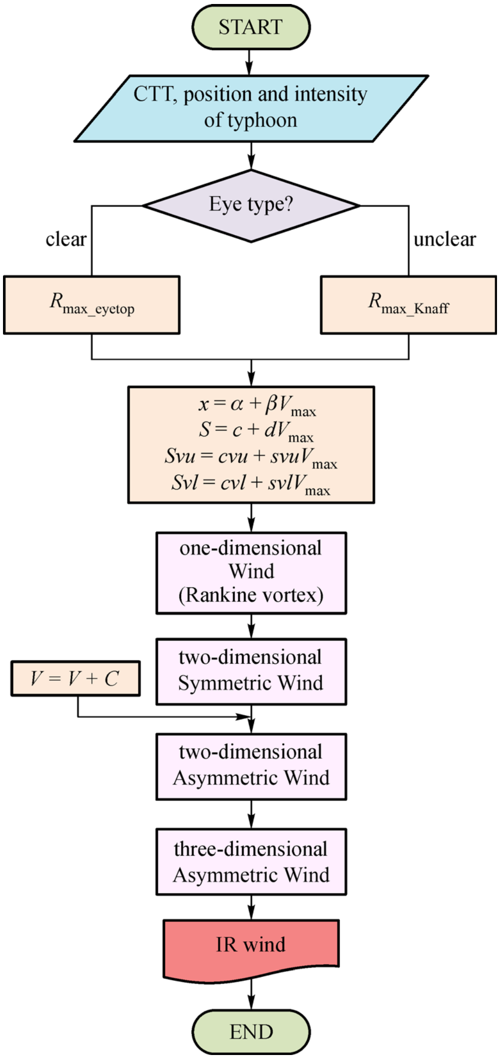

Fig. 2 Flow chart for geostationary IR image-based typhoon wind (IR wind).

where, r is the distance from the typhoon center, V is the tangential wind speed, V_{max} is the maximum wind speed (or typhoon intensity), R_{max} is the radius of the maximum wind speed, and x is the relaxation coefficient. R_{max} is determined in two ways. When the typhoon's eye was clearly discernible from the image, it was determined using the equation below, referred to as the $R_{\mathrm{max\_eyetop}}$ Method:

$$R_{\mathrm{max}}=(1-h)R_{\mathrm{TOP}}+hR_{\mathrm{EYE}}, \tag{2}$$

where, R_{TOP} is the distance in kilometers from the typhoon center to the location of the minimum CTT, R_{EYE} represents the eye size in kilometers, and h is an empirical constant of 0.6 (Lajoie and Walsh, 2008). When the eye was not clear from the IR image, R_{max} was determined as a function of input V_{max} and latitude (φ) using an empirical relationship (residual sum of squares of regression analysis based on historical aircraft observations are 0.30 and 0.98 for climatological and binned average R_{max}; Knaff et al., 2015) statistically derived from hurricane cases ($R_{\mathrm{max\_Knaff}}$ Method):

$$\begin{aligned} R_{\mathrm{max}} &= 404.4368-4.3250V_{\mathrm{max}} \\ &\quad +0.0580V_{\mathrm{max}}^{2}-3.0911 \\ &\quad \times 10^{-4}V_{\mathrm{max}}^{3}-269.4827\cos\varphi. \end{aligned} \tag{3}$$

Then, x was statistically estimated as a linear function of V_{max}, e.g., $x=\alpha+\beta V_{\mathrm{max}}$ ($\alpha=0.1300$ and $\beta=0.0108$ s/m), from historical typhoon cases of ECMWF–YOTC from 2008 to 2010 (residual sum of squares of regression analysis with the best track V_{max} data are 0.30 and 0.95 for climatological and binned average x, Fig. 4(a)). The vertical rate of change in the radius of maximum wind, S, e.g., $R_{\mathrm{max}}(z)=SR_{\mathrm{max}}(z=1000\ \mathrm{hPa})$, was also statistically estimated as a linear function of V_{max} as $S=c+dV_{\mathrm{max}}$ ($c=-0.0108$ km/hPa and $d=-0.0009$ km/hPa/(m/s)) from the typhoon cases (the residual sum of squares of regression analysis with the best track $V_{\max}$ data are 0.18 and 0.71 for climatological and binned average S, Fig. 4(b)). Similarly, vertical rates of changes in maximum wind above or at 850 hPa (Svu) and below or at 900 hPa (Svl), i.e., $V_{\max}(z) = SvlV_{\max}(z = 1000\text{ hPa})$ for lower levels with pressure levels $\geqslant$900 hPa and $V_{\max}(z) = SvuV_{\max}(z = 900\text{ hPa})$ for upper levels with pressure levels $\leqslant$850 hPa, were estimated as $Svl = cvl + dvlV_{\max}$ and $Svu = cvu + dvuV_{\max}$, respectively. Here, the regressions provided $cvu = -0.0053$ m/s/hPa, $dvu = +0.0008$ /hPa, $cvl = +0.0306$ m/s/hPa, and $dvl = -0.0060$ /hPa (the residual sum of squares of regression analysis with the best track $V_{\max}$ data are 0.62 and 0.47 for climatological Svl and Svu, and 0.96 and 0.93 binned average Svl and Svu, Figs. 3 (b) and 4(c)). Then, the two-dimensional symmetric field of $V(r)$ constructed using Eq. (1) from $V_{\max}$ (input), $R_{\max}$, and x was extended to the three-dimensional symmetric field of $V(r,z)$ from S, Svu, and Svl. Finally, the translation speed of the typhoon (C), which was calculated from changes in the center position using the best track data, was inserted to the three-dimensional symmetric field to produce the three-dimensional asymmetric field ($V + C$) of horizontal winds in and around the typhoon as the IR wind product (Fig. 2).

3.2 Typhoon wind modified using microwave sounder data (MW wind)

When available in the typhoon-centric domain of the 10° × 10° area within a time window of 12 h, the brightness temperature data in the two channels of AMSU were utilized to incorporate the typhoon's warm core structure (Fig. 5). The warm core sizes at two levels ($R7$ and $R8$) corresponding to channels 7 and 8 were estimated as the radii from the typhoon center to the radial location, where the temperature is 0.5°C lower than that at the center. The difference between the two warm core sizes ($R8$ minus $R7$) was used to correct the vertical rates of change in the radius of maximum wind ($S_{R_{\max}}$) and maximum wind ($S_{V_{\max}}$) from the regression analysis of 133 typhoon cases of the ECMWF-YOTC reanalysis data (Fig. 6):

$$S_{R_{\max}} = l + \frac{m(R8 - R7)}{100},\ S_{V_{\max}} = i + \frac{j(R8 - R7)}{100}. \tag{4}$$

Here, regression coefficients, l, m, i, and j were determined to be −0.0639 (km/hPa), 0.0341 (/hPa), 0.0134 ((m/s)/hPa), and −0.0046 ((m/s)/hPa/km), respectively (residual sum of squares of regression analysis with the typhoon cases are 0.61 and 0.69 for binned average $S_{R_{\max}}$ and $S_{V_{\max}}$). The IR wind was modified with updated $R_{\max}(z)$ and $V_{\max}(z)$ using the warm core structure observed from the microwave sounder when available to produce the MW wind.

3.3 Typhoon wind merged from multi-satellite data (MT wind)

Feature-tracked AMVs from geostationary satellites (COMS), mostly available at the upper levels around the typhoons, are useful for constructing more realistic typhoon winds. However, realistic AMVs around the typhoon are removed during general quality control processing due to its rotational characteristic; typically, AMVs with a quality index higher than 0.85 are not used for non-typhoon application. To include more AMVs around the typhoon, thresholds for the quality index were

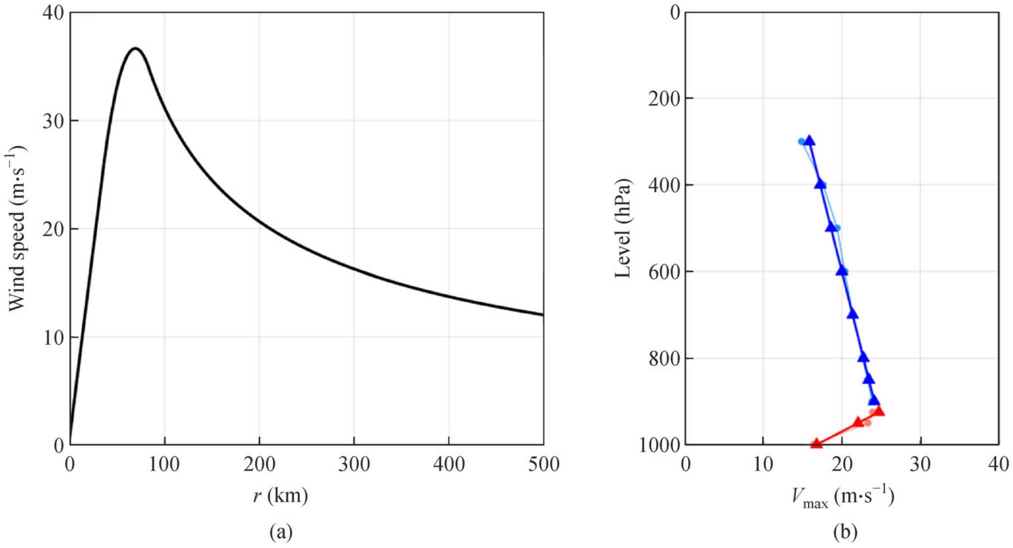

(a) (b)

Fig. 3 (a) Radial profile of tangential wind speed from the modified Rankine vortex model as a function of distance r from the typhoon center. (b) Vertical profile of maximum wind speed $V_{\max}$ as a function of height pressure level in hPa (z). Red and blue lines show linear fits below or at 900 hPa (lower levels) and above or at 850 hPa (upper levels).

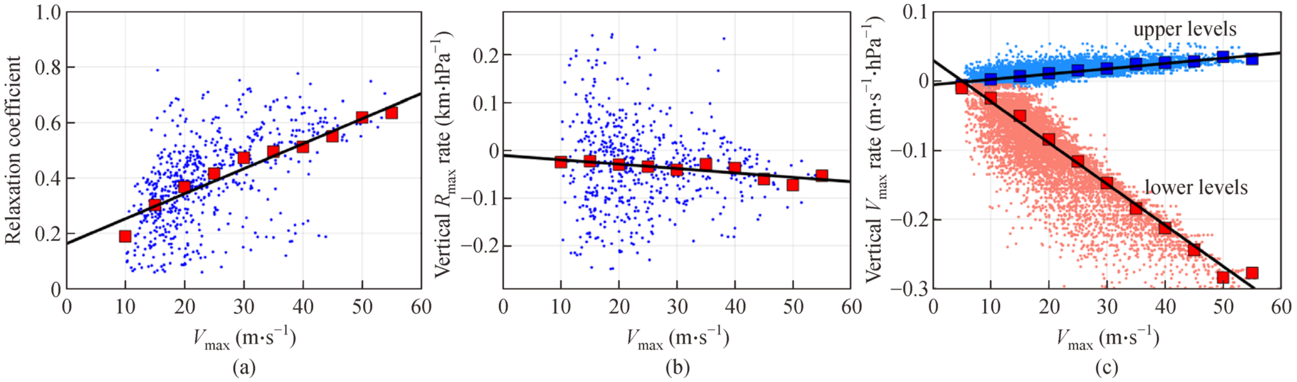

Fig. 4 (a) Relaxation coefficient (*x*), and vertical rates of change in (b) radius of maximum wind (*S*) and (c) maximum wind (*Svl* and *Svu*). Boxes and lines indicate binned data and regression fits, respectively.

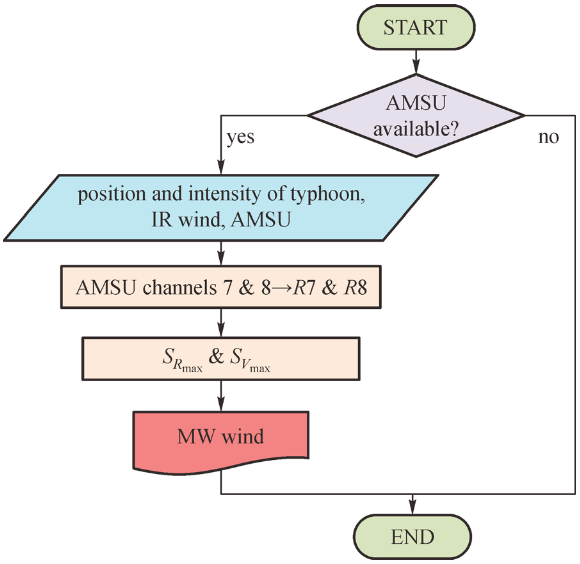

Fig. 5 Flow chart for passive microwave sounder-based typhoon wind (MW wind).

changed to 0.50 (Fig. 7). Equally important SSWs can be obtained from the scatterometer when available nearby the typhoon center. Thus, the ASCAT data available in the typhoon-centric domain of the 10° × 10° area within a time window of 12 h, along with continuous geostationary satellite AMVs, were used to construct the final typhoon wind product from IR wind and MS wind, which is referred to as MT wind (Fig. 8). Thus, MT wind was constructed from 1) geostationary-satellite-based feature-track AMVs, 2) infrared-image (CTT)-based IR wind, 3) microwave-sounder (AMSU or others of similar kinds)-based MW wind, and 4) scatterometer (ASCAT or others of similar kinds)-based SSW by synchronizing the typhoon center determined using the circular variance (CV) method (Park et al., 2016).

Weights of individual typhoon winds as functions of *r* and *z* ($W_{r\_i}(r)$ and $W_{z\_i}(z)$, where *i* is *ASCAT*, *AMV*, *IR*, or *MW* for scatterometer-based SSW, feature-tracked AMVs, IR wind, or MW wind, respectively) were necessary to merge the four kinds of typhoon winds to produce the final MT wind products. In general, it is ideal to make the weight inversely proportional to the root-mean-squared error (RMSE); yet, the AMV error does not depend on *r* but *z*, only yielding the minimum error at ~300 hPa. Using the RMSE obtained from the historical typhoon cases of ECMWF-YOTC reanalysis data and considering the

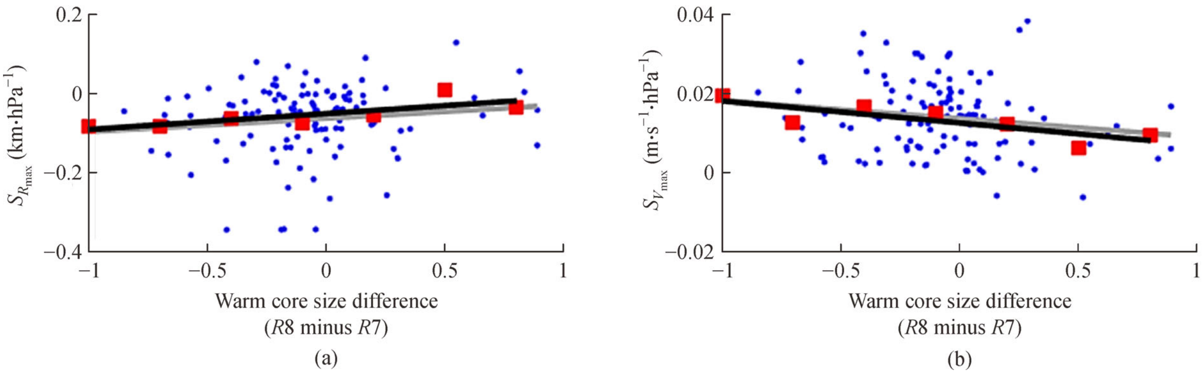

Fig. 6 Vertical rates of change in radius of maximum wind ($S_{R_{\max}}$) and maximum wind ($S_{V_{\max}}$) as a function of difference in warm core sizes in two channels (*R*8 minus *R*7). Red boxes and black lines indicate binned data and regression fits, respectively.

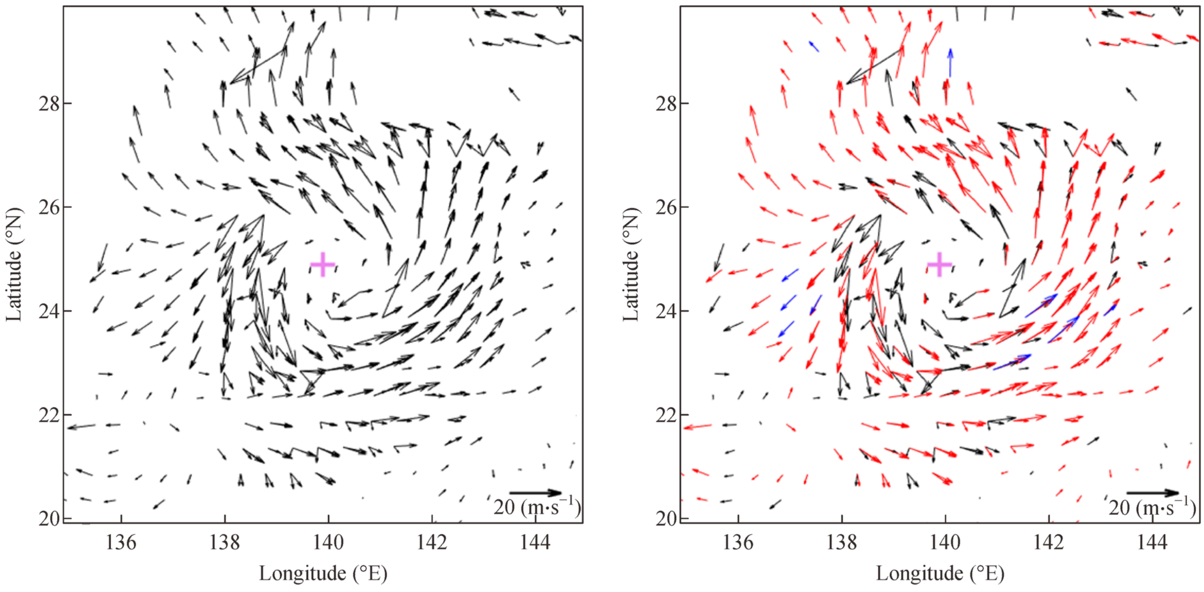

(a) (b)

Fig. 7 Examples of (a) raw and (b) quality-controlled water vapor channel AMVs obtained from geostationary satellite COMS in and around Typhoon Soulik between 100 and 200 hPa. In (b), blue and red arrows show AMVs with a quality index higher than 0.85 and 0.50, respectively. Pink crosses indicate the typhoon center.

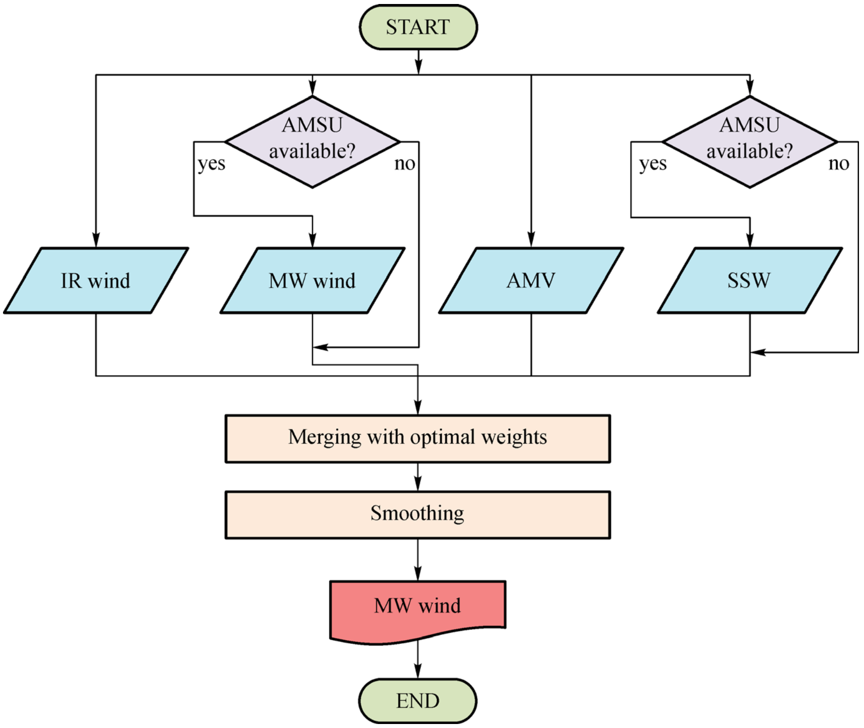

Fig. 8 Flow chart for merging typhoon winds from multi-platform satellite data (MT wind).

characteristics of the individual typhoon wind, $W_{r\_i}(r)$ and $W_{z\_i}(z)$ were determined as $W_{r\_\mathrm{ASCAT}}(r)=\frac{\min(\mathrm{RMSE})}{\mathrm{RMSE}}$, $W_{r\_\mathrm{AMV}}(r)=1$, $W_{r\_\mathrm{IR}}(r)=W_{r\_\mathrm{MW}}(r)$ $=\begin{cases} 1-\frac{r}{300} & (0\leqslant r\leqslant 300\ \mathrm{km}) \\ 0 & (r\geqslant 300\ \mathrm{km}) \end{cases}$, $W_{z\_\mathrm{ASCAT}}(z)$ $=\begin{cases} 1 & (z=1000\ \mathrm{hPa}) \\ 0 & (z\neq 1000\ \mathrm{hPa}) \end{cases}$, and $W_{z\_\mathrm{AMV}}(z)=W_{z\_\mathrm{IR}}(z)$

$=W_{z_{\mathrm{MW}}}(z)=\frac{\min(\mathrm{RMSE})}{\mathrm{RMSE}}$ for the four typhoon winds (Fig. 9). To minimize the artificial effects of discontinuities around the boundary of the swath of polar-orbit satellites and sparse AMVs, wind speeds exceeding 100 m/s were removed, and the azimuthal-mean tangential winds were smoothed using radial and azimuthal window sizes of 15 km and 45°, respectively. The final output of MT wind was produced as gridded data with a horizontal resolution of 0.1° and 11 standard pressure levels (100, 150, 200, 250, 300, 400, 500, 700, 850, 925, and 1000 hPa, where 1000 hPa represents the height of 10 m above sea level) in the typhoon-centric domain of the 10° × 10° area.

4 Application to Typhoon Soulik (2018)

Typhoon Soulik was one of the strongest storms of the typhoon season when developed in the Pacific. It formed as a tropical depression near Palau and intensified into a tropical storm, after which it rapidly intensified into a typhoon. Typhoon Soulik rapidly decayed over the northern East China Sea, while its intensity was over-predicted just before it made landfall on the Korean Peninsula (Park et al., 2019).

4.1 Open ocean (Case A)

Typhoon Soulik maintained its high intensity over the open ocean before approaching the Korean Peninsula, and its minimum pressure and intensity were 955 hPa (Fig. 1(a)) and 41 m/s (Fig. 1(b)), respectively, at 12:00 UTC on 18 August 2018 (Case A). As the eye was clear from the COMS IR image, the $R_{\mathrm{max\_eyetop}}$ Method was applied to yield $R_{\max} = 54$ km, $x = 0.58$, $S = -0.0470$ km/hPa, $Svu = 0.0276$ m/s/hPa, and $Svl = -0.2163$ m/s/hPa from the input $V_{\max}$ of the best track data (41 m/s). Then, the IR wind was obtained by adding the speed (3.5 m/s) and direction (266°; rotated clockwise from north) of the translation speed to the symmetric wind field estimated from these parameters (Fig. 10(a)). The IR wind was modified using the two channel AMSU-A data to produce the MW wind with $S_{R_{\max}} = -0.0654$ km/hPa and $S_{V_{\max}} = 0.0136$ m/s/hPa, respectively, although modification occurred mostly in the upper levels in association with the warm core (Fig. 10(b)). As the swath of MetOp-A ASCAT was within the typhoon-centric domain of the 10° × 10° area (Fig. 10(c)), scatterometer-based SSWs along with the feature-tracked COMS AMVs were incorporated into MT wind (Fig. 10(d)). MT wind was validated against the SAR-based SSWs (Fig. 10(f)) and the AMSR2-based SSW speeds (Fig. 10(g)), particularly in comparison to the ERA5 reanalysis wind (Fig. 10(e)).

The areas of strongest SSW and significant veering from the tangential wind around the typhoon center mismatched, particularly in the area of high rainfall intensity (Figs. 11(a) and 11(c)). Nevertheless, radial profiles of wind speed as a function of distance from the typhoon center were consistent between MT wind and SAR wind (Fig. 11(b)), yielding output $V_{\max}$ of 26 and 24 m/s, respectively, which were commonly and significantly lower than the input best track $V_{\max}$ (41 m/s), AMSR2 $V_{\max}$, and higher than the ERA5 reanalyzed $V_{\max}$ (Table 2). The RMSEs of MT wind speed, with reference to SAR and AMSR2 wind speeds, were 0.8 and 2.3 m/s, respectively. Although ASCAT slightly overestimated wind speed inside the eye ($r < R_{\max}$) with reference to SAR wind, MT wind showed a higher agreement with SAR wind inside the eye because the ASCAT wind speed was compensated by under-estimated IR and MW winds, which have greater weights (W_{r_IR} and $W_{r\_\mathrm{MW}} > W_{r\_\mathrm{ASCAT}}$) closer to the eye (Fig. 9(a)). The resulting $R_{\max}$ and radius of 15 m/s ($R15$) of MT

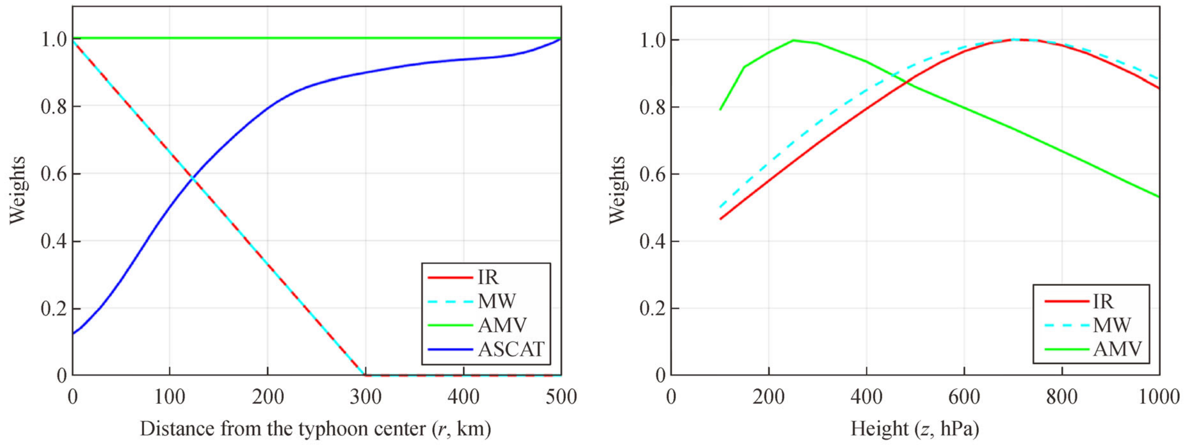

(a) (b)

Fig. 9 Weighting functions according to (a) distance from the typhoon center and (b) altitude level for four kinds of typhoon winds: infrared-image-based wind (IR, red), microwave-sounder-based wind (MW, cyan), geostationary satellite feature-tracked AMVs (AMV, green), and scatterometer-based SSW (ASCAT, blue).

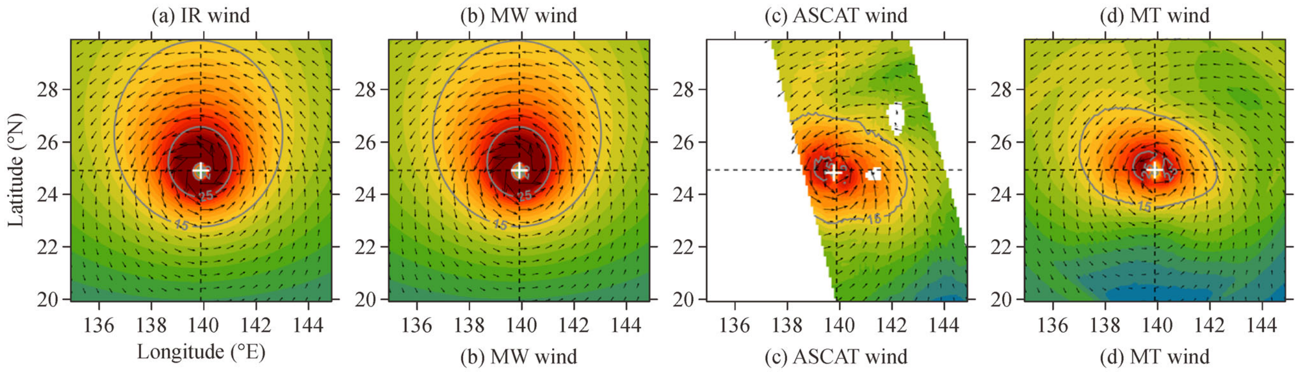

(a) IR wind (b) MW wind (c) ASCAT wind (d) MT wind

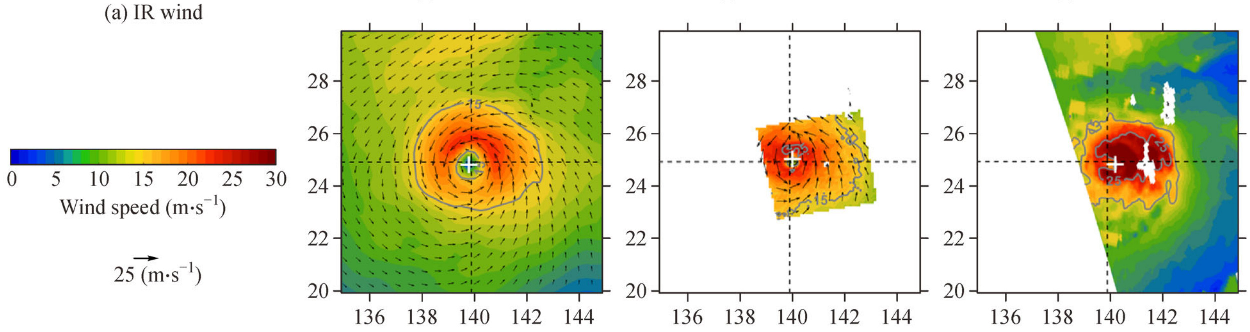

(e) ERA5 wind (f) SAR wind (g) AMSR2 wind

Fig. 10 Wind speed (color contour) and wind vector (black arrows) at the height of 10 m above sea level of (a) IR wind, (b) MW wind, (c) ASCAT wind, (d) MT wind, (e) ERA5 wind, (f) SAR wind, and (g) AMSR2 wind for Case A. Typhoon centers based on the best track data and CV method are marked by black dashed lines and white crosses. The gray contours denote wind speeds of 15 and 25 m/s.

wind were 58 and 224 km, which were close to those of SAR wind (53 and 244 km respectively, Table 2) and AMSR2 wind (56 and 218 km respectively, Table 2), suggesting that the output typhoon wind was more realistic than that of ERA5 and may be practically useful. Note that ERA5 had lower performance, which significantly underestimated wind speed within 100 km from the center, yielding a highly overestimated $R_{\max}$ of 102 km (Table 2, Fig. 11(b)).

4.2 Marginal sea before landing (Case B)

Typhoon Soulik rapidly weakened just before landing on the Korean Peninsula. Its severity was over-predicted, with a minimum pressure and intensity of 972 hPa (Fig. 1(a)) and 32 m/s (Fig. 1(c)), respectively, at 09:00 UTC on 23 August 2018 (Case B). As the eye was not clear from the COMS IR image, in contrast to Case A, the $R_{\max\_\mathrm{Knaff}}$ Method was applied to yield $R_{\max} = 124$ km, $x = 0.48$, $S = -0.0387$ km/hPa, $Svu = 0.0202$ m/s/hPa, and $Svl = -0.1608$ m/s/hPa from the input $V_{\max} = 32$ m/s of the best track data. Then, the IR wind was obtained by adding the speed (1.5 m/s) and direction (175°; rotated clockwise from north) of translation speed to the symmetric wind field estimated from these parameters (Fig. 12(a)). Similar to Case A, the IR wind was modified using the AMSU-A brightness temperature data in channels 7 and 8 to produce MW wind with $S_{R_{\max}} = -0.0503$ km/hPa and $S_{V_{\max}} = 0.0116$ m/s/hPa, respectively (Fig. 12(b)). As the swath of MetOp-B ASCAT was within the typhoon-centric domain of the 10° × 10° area (Fig. 12(c)), scatterometer-based SSWs along with feature-tracked COMS AMVs were incorporated into MT wind (Fig. 12(d)). Unlike Case A, however, the ASCAT data were mostly masked by land. Consequently, the resultant MT wind was not well validated against SAR-based SSWs (Fig. 12(f)), showing a poorer estimation skill than ERA5 reanalysis wind (Fig. 12(e)).

Although rainfall intensity was weaker than in Case A, the veering of SSWs from the tangential wind was remarkable (Figs. 11(d) and 11(f) vs 11(a) and 11(c)), and the speed profile of MT wind was significantly overestimated for $r > 81$ km (Fig. 11(e)), yielding an output $V_{\max}$ of 24 m/s, which was still lower than the input best track data but noticeably higher than ERA5 reanalyzed wind, SAR wind, and ASCAT wind (Table 2). This is because the overestimated IR and MW winds due to the over-predicted typhoon intensity (stick to higher input $V_{\max}$), with resultant long $R_{\max}$ derived from the $R_{\max\_\mathrm{Knaff}}$ Method, were not effectively corrected owing to the largely land masked ASCAT. Thus, MT wind could not estimate SSWs reasonably (Fig. 11(e)). The resultant $R_{\max}$ and $R15$ of MT wind were 135 and 340 km, which were much higher than those of SAR wind (109 and 197 km respectively, Table 2), ASCAT or ERA5, suggesting that caution is required when using the estimated typhoon

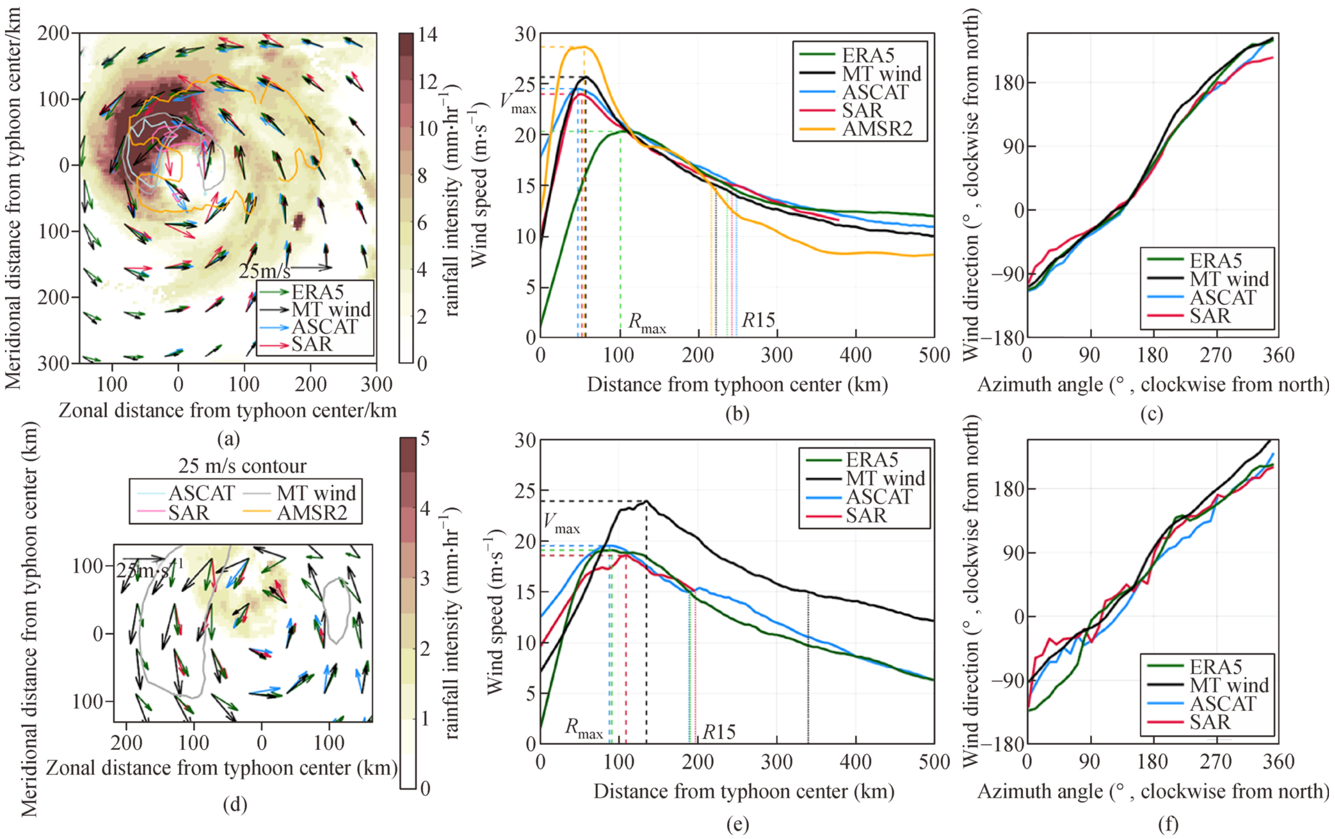

Fig. 11 (a, d) COMS rainfall intensity (color, mm/h), ERA5 reanalyzed wind (green), MT wind (black) ASCAT wind (blue), and SAR wind (red). Colored contours denote a wind speed of 25 m/s. (b, e) Radial profile of tangential wind speed as a function of distance from the typhoon center, and (c, f) wind direction in degrees rotated clockwise from the north as a function of azimuth angle, from ERA5 reanalyzed wind (green), MT wind (black), ASCAT wind (blue), SAR wind (red), and AMSR2 wind (orange) for (a–c) Case A and (d–f) Case B.

Table 2 Maximum wind (V_{max}, m/s), radius of maximum wind (R_{max}, km), and radius of 15 m/s ($R15$, km) of azimuthally averaged tangential wind from MT wind, ASCAT, SAR, ERA5, AMSR2, and best track for Cases A and B. Here, the best track $R15$ was obtained by averaging the maximum and minimum radius of 15 m/s

	Case A						**Case B**					
	MT wind	ASCAT	SAR	ERA5	AMSR2	Best track	MT wind	ASCAT	SAR	ERA5	AMSR2	Best track
V_{max} (m/s)	26	24	24	21	28	41	24	20	18	19		32
R_{max} (km)	58	48	53	102	56	Not applicable	135	88	109	91	Not applicable	Not applicable
$R15$ (km)	224	250	244	238	218	305	340	190	197	190		264

wind, particularly when the typhoon intensity (input V_{max}) is over-predicted before landing.

5 Discussion

5.1 SSW speed

Radial profiles of SSW speed could be reasonably estimated from the developed algorithm for Case A, yielding relatively small (~2 m/s) discrepancies of output V_{max} (Table 2). Small RMSE of MT wind speed with reference to SAR wind speed (0.8 m/s, Fig. 11(b)), considering comparable typical errors of SAR wind (~2.0 m/s, Moon et al., 2010) and comparable RMSE of MT wind speed with reference to AMSR2 wind speed (2.3 m/s, Fig. 11(b)), demonstrates promising results for the estimation of realistic typhoon winds to better monitor

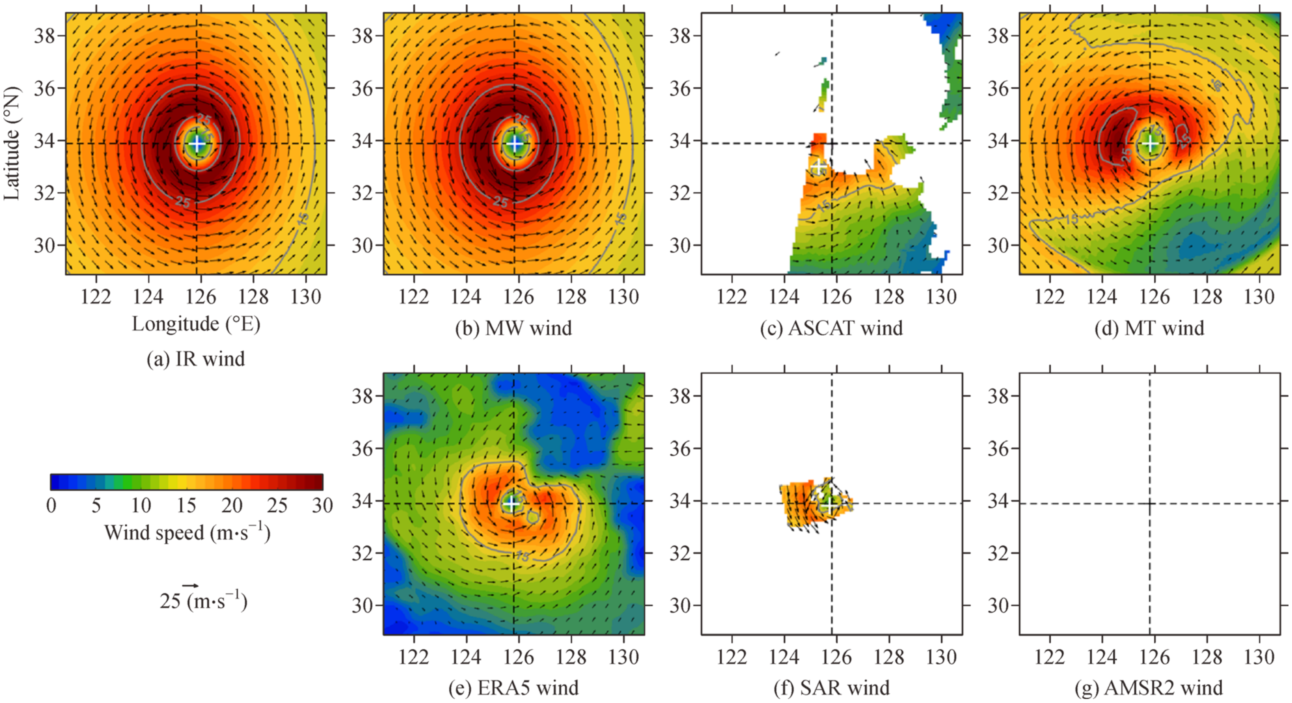

(a) IR wind (b) MW wind (c) ASCAT wind (d) MT wind (e) ERA5 wind (f) SAR wind (g) AMSR2 wind

Fig. 12 Wind speed (color contour) and wind vector (black arrows) at the height of 10 m above sea level of (a) IR wind, (b) MW wind, (c) ASCAT wind, (d) MT wind, (e) ERA5 wind, (f) SAR wind, and (g) AMSR2 wind for Case B. Typhoon centers based on the best track data and CV method are marked by black dashed lines and white crosses. The gray contours denote wind speeds of 15 and 25 m/s.

and predict typhoons using real-time satellite data only. The wind speed profiles of ASCAT, MT wind, AMSR2, and SAR were consistent and more reasonable than those of ERA5, where the latter could not reproduce the strong maximum wind associated with Typhoon Soulik for Case A (Fig. 11(b)). In spite of the mismatched strongest SSW sector with AMSR2, the $R_{\max}$ and R15 of AMSR2 were also closer to those of MT wind than ERA5 (Figs. 11(a) and 11(b)). Further improvements can be made by correcting the effects of rainfall on the scatterometer-based SSW speed. Even though the C-band ASCAT is relatively robust to rain contamination, the ASCAT wind speed can still be slightly over- or underestimated by a few meters per second, depending on wind speed and rainfall intensity, as reported by Ricciardulli and Wentz (2014) and shown in Fig. 13. The positive bias in the wind speed difference (ASCAT wind speed minus SAR wind speed) for rain-free conditions can either be due to an overestimated ASCAT wind speed or an underestimated SAR wind speed (black in Fig. 13). Strong veering of SSWs from the tangential wind (nonzero radial component) was observed in the northwestern sector, where rainfall intensity was highest (Fig. 11(a)). The strongest SAR wind found in the northern sector could not be well resolved by ASCAT and MT wind, most likely due to rain contamination (Portabella et al., 2012b; Chou et al., 2013; Ricciardulli and Wentz, 2014).

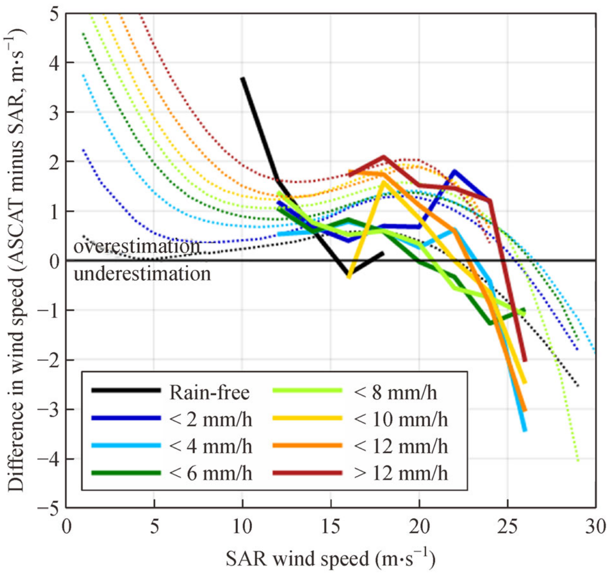

Fig. 13 Difference (ASCAT minus SAR) in wind speed derived from ASCAT and SAR as a function of SAR wind speed for rain-free (black solid line) and rain-contaminated cases (colored solid lines) of Case A. The known tendency of the over- and underestimation ASCAT bias error is denoted with colored dashed lines based on a previous work by Ricciardulli and Wentz (2014).

The C-band microwave observations (AMSU-A, ASCAT, and SAR) will be to some extent saturated when wind speeds are above 25 m/s or under rainy conditions. The rain effect, in particular, is considered in the atmosphere column and on the ocean surface (Zhang et al., 2016). Attenuation and volume backscattering for microwave transfer in the atmosphere is negligible for VV polarization, but these effects should be important at very low wind speeds, and the VV polarized normalized radar-backscatter cross section would increase for volume backscattering (Zhang et al., 2016). The rain-induced damping on wind waves and rain-generated ring waves on the ocean surface can be neglected for C-band VV polarization, but non-Bragg scattering is important for the cross-polarized normalized radar-backscatter cross section (Zhang et al., 2016). In general, the wind speed regime in which this effect occurs (Huang et al., 2017; Zhang et al., 2017) would be at SSW speeds exceeding 30 m/s. In this study, though, most of the SSW speeds were below 30 m/s, so that VV polarization was used without considering the saturation issue. Instead, the SSW speeds were validated with AMSR2, which better estimated wind speeds under extended saturated conditions than C-band microwave observations. ASCAT and SAR underestimated wind speeds with reference to AMSR2 wind speeds, particularly, in $V_{\max}$ and $R_{\max}$.

However, the developed algorithm needs to be cautiously applied when the typhoon intensity is over-predicted in the marginal sea before landing, as demonstrated in Case B. The algorithm can significantly overestimate SSW speed for $r > 81$ km (Fig. 11(e)), even with weak rainfall intensity because of the noticeably high $V_{\max}$ derived from the input $V_{\max}$ and larger $R_{\max}$ derived from the $R_{\max\_\text{Knaff}}$ Method of IR wind. Note that the typhoon intensity (input $V_{\max}$) was over-predicted, and the rapid decay of Typhoon Soulik over the northern East China Sea before landing (Park et al., 2019) could not be incorporated. Unlike Case A, the overestimated IR and MW winds were not effectively corrected by ASCAT wind, as the scatterometer measurements were severely masked by land in the vicinity of the typhoon center (Figs. 10(c) and 12(c)).

To validate the vertical structure, vertical profiles of MT wind speed were compared with those of ERA5 and dropsonde observations. The MT wind speeds at the location of the dropsonde observations in case of Typhoon Megi were significantly higher than the ERA5 wind speeds (matching the dropsonde observation as assimilated) at all levels (blue vs red and black circles in Fig. 14(a)). However, relatively small (~4 m/s) discrepancies were found for Case A between MT and ERA5 wind speeds after averaging over the range within R15 (blue vs red squares in Fig. 14(a)). Thus, the estimation of the vertical wind speed structure around the typhoon by the developed algorithm was clearly limited, though reasonable, in terms of the spatial average, and further improvements are required utilizing more and better AMVs in the future.

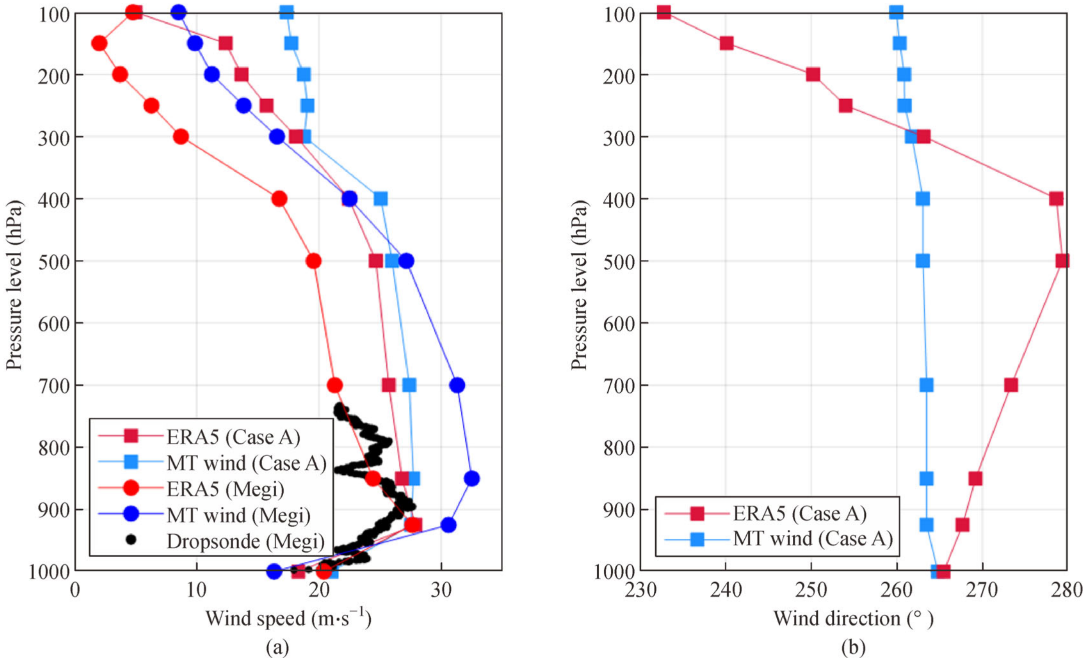

Fig. 14 (a) Mean vertical profiles of wind speed of ERA5 wind (red squares) and MT wind (blue squares) within R15 for Case A and vertical profiles of wind speeds at a dropsonde observation location of ERA5 wind (red circles), MT wind (blue circles), and dropsonde wind (black circles) for typhoon Megi. (b) Wind direction (angle measured clockwise from the north) of ERA5 wind (red squares) and MT wind (blue squares) within R15 for Case A.

5.2 SSW direction

As IR and MW winds are based on the modified Rankine vortex model, the winds are purely tangential and have no radial component. Thus, the veering from the tangential wind of MT wind originated from ASCAT SSWs and COMS AMVs. MT wind, SAR wind, and ERA5 reanalyzed wind as well as SSWs and AMVs also showed significant veering from the tangential wind (departure from the linear line in Figs. 11(c) and 11(f)). While the veering of MT wind somewhat agreed with those of ASCAT wind, SAR wind, and ERA5 wind for Case A, the discrepancies among the typhoon winds were significantly higher for Case B, in spite of weaker rain contamination of ASCAT wind (Figs. 11(c) and 11(f)). This implies that the direction error is more likely related to typhoon intensity than rainfall intensity. The vertical profile of the MT wind direction averaged over the area within R15 was also significantly ($>10°$) different from that of ERA5 wind for Case A (Fig. 14(b)). The ERA5 wind direction decreased (rotates counter-clockwise) upward in the upper levels (<500 hPa) and downward in the lower levels (>500 hPa), while the MT wind direction remained nearly constant at ~263° close to the typhoon translation direction (266°), reflecting that further improvements of the algorithm for asymmetric winds would be possible. The developed algorithm is clearly limited by the ability to reproduce wind veering associated with the additional complexity of typhoons imposed by friction and boundary layer processes that may become significant when approaching land. Further improvements of the developed algorithm need to consider these factors.

5.3 Typhoon size ($R_{\max}$ & $R15$)

In Case A, $R_{\max}$ was estimated to be 48–58 km by all but ERA5 reanalyzed wind (102 km), and $R15$ was estimated to be 218–250 km, which was noticeably smaller than the best track data (305 km) by all typhoon winds. This implies that the proposed algorithm has practical use in monitoring realistic typhoon wind more accurately than existing techniques within a 10–26 km of discrepancy in typhoon size (Table 1). However, in Case B, the proposed algorithm appeared to overestimate $R_{\max}$ (135 km) and $R15$ (340 km), considering that $R_{\max}$ and $R15$ of the other satellite products ranged from 88 to 109 km and from 190 to 197 km. In particular, $R15$ estimated by the algorithm was even larger than the over-predicted best track data (264 km), thus, suggesting caution when applied to typhoons in the vicinity of land. This systematic overestimation problem can be largely alleviated when either of the following conditions is satisfied:

1) The typhoon's eye is sufficiently clear to apply the $R_{\max\_\text{eyetop}}$ Method.

2) Typhoon intensity is sufficiently well predicted to input a realistic $V_{\max}$.

3) SSW within the swath of scatterometers (ASCAT or others of similar kinds) in the vicinity of the typhoon center is not largely masked by land.

4) SSW from C-band microwaves is appropriately retrieved under the conditions of strong rainfall or high wind.

6 Concluding remarks

An algorithm was developed to monitor horizontal wind in and around typhoons in real-time using multi-satellite data and applied to Typhoon Soulik (2018). Geostationary satellite infrared image-based typhoon wind (IR wind) was estimated from statistical relationships of parameters (x, $R_{\max}$, S, Svu and Svl) derived from 646 historical typhoon cases, including typhoon intensity (input $V_{\max}$) using the modified Rankine vortex model. When microwave sounder data were available in the typhoon-centric domain ($10° \times 10°$) within the time window (12 h), IR wind was modified using statistical relationships with the warm core sizes within the channels of passive microwave sounder data (MW wind). Then, scatterometer-derived SSW vectors and geostationary-satellite-imager-derived feature-tracked AMVs were merged into the final product of typhoon wind (MT wind) using optimized weights as functions of the height and distance from the typhoon center. The developed algorithm was applied to two cases of Typhoon Soulik and validated against the SSW field, independently extracted from active SAR (SAR wind) and passive AMSR2 (AMSR2 wind), and vertical profiles of wind speed obtained from reanalyzed wind and dropsonde observations. MT wind provided reasonable and practically useful estimates of maximum wind (output $V_{\max}$), maximum wind radius ($R_{\max}$,), and radius of 15 m/s winds ($R15$), which could not be estimated using reanalysis data (ERA5). The radial and vertical wind speed profiles of MT wind were consistent with those of SAR wind, AMSR2 wind speed, dropsonde wind speed, or reanalyzed wind for the open ocean case (Case A). However, in case B, MT wind significantly overestimated $V_{\max}$, $R_{\max}$, and $R15$ because the eye was unclear in the IR image, typhoon intensity was over-predicted, and scatterometer data were largely land-masked when the typhoon rapidly weakened just before making landfall on the Korean Peninsula.

The developed algorithm allows continuous estimation of the three-dimensional wind field in and around typhoons, without any gaps in space within the typhoon-centric domain of the $10° \times 10°$ area in real-time. Timely analysis results and products of operational importance can be acquired using the proposed algorithm, with the incorporation of products from the new Korean geostationary satellite GEO-KOMPSAT-2A (GK-2A) launched in December 4, 2018 (e.g., CTTs and AMVs from the GK-

2A instead of COMS). Here, we describe the validating results of applying this algorithm to cases of Typhoon Soulik (and Typhoon Megi). Although the developed algorithm has clear limitations depending on predicted typhoon intensity, a clean eye, rainfall intensity, and conditions of landfall, its practicality and potential advantages could be demonstrated. In particular, the resulting SSWs were highly sensitive to input $V_{\max}$ or typhoon intensity and the availability (with minimized land masking) of scatterometers in the vicinity of the typhoon center within the swath. However, they were less sensitive to feature-tracked AMVs and warm-core structure-incorporated microwave sounders that mostly affect the upper level wind only. Further improvements can be made by utilizing multiple microwave imagers and sounders, multiple scatterometers, and future outputs of the Doppler wind Lidar mission Aeolus (Nam and Park, 2018), adding more factors to statistically determine typhoon wind parameters beyond typhoon intensity and correcting rain contamination of scatterometer-based SSWs more effectively.

Acknowledgements We would like to thank four anonymous reviewers for valuable comments and useful suggestions, and Editage for English language editing, and give special thanks to John Knaff, MyeongHee Han, Minho Kwon, Il-Ju Moon, and Chu-Yong Chung for advice and discussions on developing the algorithm. The best track data sets were obtained from the Regional Specialized Meteorological Center of the Japan Meteorological Agency (available at Japan Meteorological Agency website). ECMWF-YOTC and ERA5 data are provided by ECMWF (available at ECMWF website) and Copernicus (available at Copernicus website). The COMS CTT and AMV data were provided by the National Meteorological Satellite Center, Korea Meteorological Administration (available at Korea Meteorological Administration website). NOAA15 AMSU-a data were provided by the Global Hydrology Resource Center (GHRC), one of NASA's DAACs (available at NASA website). MetOp-A and-B ASCAT data were provided by the JPL/NASA (available at JPL/NASA OPeNDAP website). This work was supported by the 'Development of Typhoon and Ocean Applications' project, funded by ETRI, which is a subproject of the 'Development of Geostationary Meteorological Satellite Ground Segment (NMSC-2019-01)' program funded by NMSC of KMA. This research was a part of the project titled "Construction of Ocean Research Station and their Application Studies" funded by the Ministry of Oceans and Fisheries in republic of Korea.

Electronic supplementary material is available in the online version of this article at http://dx.doi.org/10.1007/s11707-020-0849-6 and is accessible for authorized users.

References

Bessho K, DeMaria M, Knaff J A (2006). Tropical cyclone wind retrievals from the advanced microwave sounding unit: Application to surface wind analysis. J Appl Meteorol Climatol, 45(3): 399–415

Choi Y-S, Ho C H, Ahn M H, Kim Y M (2007). An exploratory study of cloud remote sensing capabilities of the Communication, Ocean and Meteorological Satellite (COMS) imagery. Int J Remote Sens, 28 (21): 4715–4732

Choi Y-S, Ho C H, Ahn M H, Kim Y M (2014). Remote sensing of cloud properties from the Communications, Oceanography and Meteorology Satellite (COMS) Imagery

Chou K H, Wu C, Lin S Z (2013). Assessment of the ASCAT wind error characteristics by global dropwindsonde observations. J Geophys Res D Atmospheres, 118(16): 9011–9021

CLS (2019). Sentinel-1 Level 1 Detailed Algorithm Definition, Document Number: SEN-TN-52–7445, Issue 2.2

Demuth J L, DeMaria M, Knaff J A, Vonder Haar T H (2004). Evaluation of advanced microwave sounding unit tropical-cyclone intensity and size estimation algorithms. J Appl Meteorol, 43(2): 282–296

Demuth J L, DeMaria M, Knaff J A (2006). Improvement of advanced microwave sounding unit tropical cyclone intensity and size estimation algorithms. J Appl Meteorol Climatol, 45(11): 1573–1581

EUMETSAT (2019). ASCAT Wind Product User Manual, version 1.16. 1–23

Figa-Saldaña J, Wilson J J W, Attema E, Gelsthorpe R, Drinkwater M R, Stoffelen A (2002). The advanced scatterometer (ASCAT) on the meteorological operational (MetOp) platform: a follow on for European wind scatterometers. Can J Rem Sens, 28(3): 404–412

Huang L, Liu B, Li X, Zhang Z, Yu W (2017). Technical evaluation of Sentinel-1 IW mode cross-pol radar backscattering from the ocean surface in moderate wind condition. Remote Sens, 9(8): 854

IFREMER-CERSAT (1996). Off-line wind scatterometer ERS products: user manual, Technical Report C2-MUT-W-01–1F, Version 2.0, IFREMER-CERSAT, BP 70, 29280 PLOUZANE, France

Kim S, Ou M L (2013). Retrieval of mesoscale atmospheric motion vectors using COMS images at KMA/NIMR. In: International Geoscience and Remote Sensing Symposium. Melbourne: IEEE, 558–561

Knaff J A, Demaria M, Molenar D A, Sampson C R, Seybold M G (2011). An automated, objective, multiple-satellite-platform tropical cyclone surface wind analysis. J Appl Meteorol Climatol, 50(10): 2149–2166

Knaff J A, Longmore S P, DeMaria R T, Molenar D A (2015). Improved tropical-cyclone flight-level wind estimates using routine infrared satellite reconnaissance. J Appl Meteorol Climatol, 54(2): 463–478

Kunitsugu M (2012). Tropical cyclone information provided by the RSMC Tokyo-Typhoon Center. Trop Cyclone Res Rev, 1: 51–59

Lajoie F, Walsh K (2008). A technique to determine the radius of maximum wind of a tropical cyclone. Weather Forecast, 23(5): 1007–1015

Mears C A, Smith D K, Wentz F J (2001). Comparison of Special Sensor Microwave Imager and buoy-measured wind speeds from 1987 to 1997. J Geophys Res Oceans, 106(C6): 11719–11729

Moncrieff M W, Waliser D E, Miller M J, Shapiro M A, Asrar G R, Caughey J (2012). Multiscale convective organization and the YOTC virtual global field campaign. Bull Am Meteorol Soc, 93(8): 1171–1187

Moon W M, Staples G, Kim D, Park S E, Park K A (2010). RADARSAT-2 and coastal applications: surface wind, waterline, and intertidal flat roughness. Proc IEEE, 98(5): 800–815

Mueller K J, DeMaria M, Knaff J, Kossin J P, Vonder Haar T H (2006). Objective estimation of tropical cyclone wind structure from infrared satellite data. Weather Forecast, 21(6): 990–1005

Nam S, Park K A (2018). Status and prospects of marine wind observations from geostationary and polar-orbiting satellites for tropical cyclone studies. J Korean Earth Sci Soc, 39(4): 305–316

Olauson J (2018). ERA5: the new champion of wind power modelling? Renew Energy, 126: 322–331

Park J H, Yeo D E, Lee K J, Lee H, Lee S W, Noh S, Kim S, Shin J, Choi Y, Nam S (2019). Rapid decay of slowly moving Typhoon Soulik (2018) due to interactions with the strongly stratified northern East China Sea. Geophys Res Lett, 46(24): 14595–14603

Park M S, Kim M, Lee M I, Im J, Park S (2016). Detection of tropical cyclone genesis via quantitative satellite ocean surface wind pattern and intensity analyses using decision trees. Remote Sens Environ, 183: 205–214

Portabella M, Stoffelen A, Verhoef A, Verspeek J (2012a). A new method for improving scatterometer wind quality control. IEEE Geosci Remote Sens Lett, 9(4): 579–583

Portabella M, Stoffelen A, Lin W, Turiel A, Verhoef A, Verspeek J, Ballabrera-Poy J (2012b). Rain effects on ASCAT-retrieved winds: toward an improved quality control. IEEE Trans Geosci Remote Sens, 50(7): 2495–2506

Ricciardulli L, Wentz F (2014). Integrating the ASCAT observations into a climate data record of ocean vector winds. In: European Geosciences Union General Assembly Conference

Sohn E H, Chung S R, Park J S (2012). Current status of COMS AMV in NMSC/KMA. In Proc. of (16–20)

Velden C S, Hayden C M, Nieman S J, Menzel W P, Wanzong S, Goerss J S (1997). Upper-tropospheric winds derived from geostationary satellite water vapor observations. Bull Am Meteorol Soc, 78(2): 173–195

Waliser D E, Moncrieff M W, Burridge D, Fink A H, Gochis D, Goswami B N, Guan B, Harr P, Heming J, Hsu H H, Jakob C, Janiga M, Johnson R, Jones S, Knippertz P, Marengo J, Nguyen H, Pope M, Serra Y, Thorncroft C, Wheeler M, Wood R, Yuter S (2012). The "year" of tropical convection (May 2008–April 2010): climate variability and weather highlights. Bull Am Meteorol Soc, 93(8): 1189–1218

Wentz F J (1997). A well-calibrated ocean algorithm for special sensor microwave/imager. J Geophys Res Oceans, 102(C4): 8703–8718

Zhang G, Li X, Perrie W, Hwang P A, Zhang B, Yang X (2017). A hurricane wind speed retrieval model for C-band RADARSAT-2 cross-polarization ScanSAR images. IEEE Trans Geosci Remote Sens, 55(8): 4766–4774

Zhang G, Li X, Perrie W, Zhang B, Wang L (2016). Rain effects on the hurricane observations over the ocean by C-band Synthetic Aperture Radar. J Geophys Res Oceans, 121(1): 14–26